Earth Planet. Sci. Lett. 628 (2024) 118584

Contents lists available at ScienceDirect

Earth and Planetary Science Letters

journal homepage: www.elsevier.com/locate/epsl

Competition or collaboration: Clay formation sets the relationship between silicate weathering and organic carbon burial in soil

Evan J. Ramos [a,b,c,*], William J. Larsen [a], Yi Hou [a], Sebastian Muñoz [c,d], Preston Cosslett Kemeny [e], Joel S. Scheingross [f], Marisa N. Repasch [g], Niels Hovius [h], Dirk Sachse [h], Daniel E. Ibarra [c,d], Mark A. Torres [a,b]

[a] Department of Earth, Environmental and Planetary Sciences, Rice University, Houston, TX 77005, USA
[b] Academy of Fellows, Rice University, Houston, TX 77005, USA
[c] Department of Earth, Environmental and Planetary Sciences, Brown University, Providence, RI 02912, USA
[d] Institute at Brown University for Environment and Society, Brown University, Providence, RI 02912, USA
[e] Department of the Geophysical Sciences, University of Chicago, Chicago, IL 60637, USA
[f] Department of Geological Sciences and Engineering, University of Nevada Reno, Reno, NV 89557, USA
[g] Institute of Arctic and Alpine Research, University of Colorado, Boulder, CO 80309, USA
[h] German Research Centre for Geosciences GFZ, 14473 Potsdam, Germany

ARTICLE INFO

Editor: H. Bao

Keywords:
organic matter stabilization
clay formation
climate change
lithium isotopes
carbon cycle

ABSTRACT

Silicate weathering and organic carbon (OC) burial in soil regulate atmospheric CO_2, but their influence on each other remains unclear. Generally, OC oxidation can generate acids that drive silicate weathering, yet clay minerals that form during weathering can protect OC and limit oxidation. This poses a conundrum where clay formation and OC preservation either compete or cooperate. Debate remains about their relative contributions because quantitative tools to simultaneously probe these processes are lacking while those that exist are often not measured in concert. Here we demonstrate that Li isotope ratios of sediment, commonly used to trace clay formation, can help constrain OC cycling. Measurements of river suspended sediment from two watersheds of varying physiography and analysis of published data from Hawaii soil profiles show negative correlations between solid-phase δ^7Li values and OC content, indicating the association of clay mineral formation with OC accumulation. Yet, the localities differ in their ranges of δ^7Li values and OC contents, which we interpret with a model of soil formation. We find that temporal trends of Li isotopes and OC are most sensitive to mineral dissolution/clay formation rates, where higher rates yield greater OC stocks and lower δ^7Li_{soil} values. Whereas OC-enhanced dissolution primarily dictates turnover times of OC and silicate minerals, clay protection distinctly modifies soil formation pathways and is likely required to explain the range of observations. These findings underscore clay mineral formation, driven primarily by bedrock chemistry and secondarily by climate, as a principal modulator of weathering fluxes and OC accumulation in soil.

1. Introduction

Earth's climate remains in a delicate balance, so much so that minor imbalances of carbon (C) inputs and outputs to the ocean and atmosphere may lead to Greenhouse or icehouse states (Berner and Caldeira, 1997). As biogeochemical hubs of C cycling that modulate and respond to climate over months to millions of years, soils play a critical role in this balance. The relevance of C cycling in soil over such a broad time span is governed by the rates of mass transfer for constitutive organic matter and inorganic (e.g., silicate) minerals in soil (Hilton and West, 2020). Organic carbon (OC), with its diversity of molecular forms and reactivity (Boudreau and Ruddick, 1991; Boye et al., 2017), rapidly cycles (< 1,000 yr) (Schmidt et al., 2011) due to quick fixation of atmospheric CO_2 by photosynthesizers, transformation to organic ligands, and mineralization to CO_2 by microbes, root exudates, mycorrhizae, or dissolved dioxygen. In contrast, silicate minerals are comparatively more stable than OC at Earth surface conditions, leading to sluggish rates of mineral dissolution and precipitation (White and Brantley, 2003; Nagy et al., 1991) with relevance to C drawdown via alkalinity generation and marine carbonate formation

* Corresponding author at: Department of Earth, Environmental and Planetary Sciences, Rice University, Houston, TX 77005, USA.
E-mail address: evan.j.ramos@rice.com (E.J. Ramos).

https://doi.org/10.1016/j.epsl.2024.118584
Received 26 July 2023; Received in revised form 9 January 2024; Accepted 14 January 2024
Available online 31 January 2024

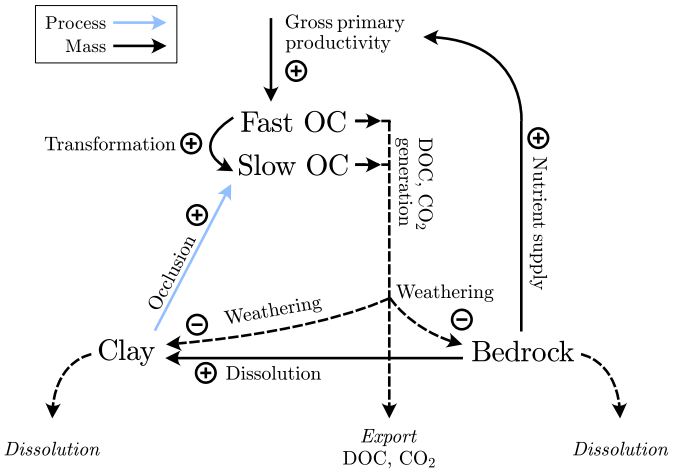

Fig. 1. Connections and feedbacks between OC cycling and silicate weathering. OC contains two reservoirs, one that is fast-cycling (particulate OC) and another that is slow-cycling (mineral associated). Silicates are composed of primary bedrock and secondary clay minerals. Solid arrows show processes that link mass transfer between reservoirs where plus signs indicate a process that increases the affected pool (i.e., one being pointed to) and minus signs indicate the opposite. We distinguish processes from mass fluxes by arrow color. Dashed arrows indicate mass loss from system.

over 10^5 to 10^6 yr (Walker et al., 1981; Berner et al., 1983). The interaction of silicate weathering and OC cycling in soil has received significant attention (Chadwick et al., 1994; Drever, 1994; Torn et al., 1997; Masiello et al., 2004; Slessarev et al., 2022; Hemingway et al., 2019; Fang et al., 2023; Roering et al., 2023) despite their distinct timescales of operation. However, it remains unclear how each process impacts one another and how environmental or geologic conditions may regulate their coupling. With increasing anthropogenic C emissions and attendant hydroclimate change (IPCC, 2022), bridging this knowledge gap in paired data sets and with quantitative modeling approaches is a pressing need (Beerling et al., 2020).

Fully characterizing the interplay of OC cycling and silicate weathering is challenging because even in an idealized system, there are several conceivable ways that they could either arrest or enhance each other (Chadwick and Chorover, 2001) (Fig. 1). For example, the breakdown of solid-phase OC generates a range of carbon species that are either exported from soil (Talbot et al., 2022) or involved in mineral dissolution and surface complexation reactions (Drever, 1994; Lawrence et al., 2014; Winnick and Maher, 2018). The enhancement of mineral dissolution by biogenic carbon species at the expense of solid OC would thus constitute a *negative* relationship between silicate weathering and OC accumulation in soil. However, the liberation of rock-bound nutrients by mineral dissolution may stimulate biological activity (Frings et al., 2021; Hahm et al., 2014; Maher and von Blanckenburg, 2023), increasing OC inputs to soil and thus generating a *positive* relationship between silicate weathering and OC accumulation in certain settings. From another perspective, not all solid OC is transformed or mineralized, and the fraction of OC that evades these processes (Spohn et al., 2016; Liang et al., 2017) persists for a longer duration (> 10,000 yr) largely because of its association with clay minerals (Chadwick et al., 1994; Torn et al., 1997; Masiello et al., 2004; Doetterl et al., 2016; Hemingway et al., 2019; Heckman et al., 2022; Fang et al., 2023) and oxides (Rasmussen et al., 2018; Tipping et al., 2002) that form in soil. The high specific surface area and negatively charged surfaces of clay minerals act as physiochemical shields from oxidants, enabling the accumulation of OC. Clay minerals are byproducts of primary silicate dissolution and in this way, their formation constitutes a *positive* relationship between silicate weathering and OC accumulation. Yet, if there is a point in soil development where OC is predominantly associated with and protected by clay minerals, the production of biogenic carbon species that enhance weathering may decrease (Schmidt et al., 2011), generating a *negative* relationship. Observations of soil profiles suggest that the nature of the coupling may depend on depth within soil (Fang et al., 2023) or soil age (Torn et al., 1997; Doetterl et al., 2016), but in considering soils in aggregate, a fundamental conundrum arises: does organic carbon cycling drive silicate weathering, or vice versa? To address this question, we argue that quantitative constraints of clay mineral formation are an essential requirement.

Conventionally, the mineralogy, physical attributes (e.g., grain size, density), or bulk chemistry of soil are used to detect clay minerals and constrain their formation rates. The difficulty of interpreting these data are that without space-for-time substitutions, which are commonly used in studies of catenas or soil chronosequences (Torn et al., 1997; Masiello et al., 2004; Lawrence et al., 2014; Doetterl et al., 2016), inferring rates of clay mineral formation and mass transfer requires highly specified, complex reactive transport models (Maher et al., 2009). Moreover, there exist quantitative bounds for measurements of bulk soil chemistry and clay mineralogy that limit the identification of new clay minerals and their corresponding formation rates. The past several decades have seen the establishment of several non-traditional stable isotope systems that have been shown to be especially sensitive to clay mineral formation, including Li isotopes (Huh et al., 1998; Dellinger et al., 2015, 2017; Andrews et al., 2020; Golla et al., 2021; Winnick et al., 2022). Clay minerals preferentially incorporate aqueous ^{6}Li over ^{7}Li during their formation (Hindshaw et al., 2019), leading to low ^{7}Li/^{6}Li ratios in clay and high ratios in the water from which it formed. The conversion of bedrock silicates to authigenic clays progressively drives soil ^{7}Li/^{6}Li to lower values and generates an empirical relationship between river suspended sediment ^{7}Li/^{6}Li and silicate weathering intensity (fraction of mass loss via weathering) (Dellinger et al., 2015, 2017), showcasing a key quantitative strength of the proxy. Studies have also illustrated the sensitivity of Li isotopes to rapid changes in clay mineral formation (Dosseto et al., 2015; Ramos et al., 2022; Chen et al., 2023). However, to our knowledge, studies have not yet explicitly paired measurements of weathering-sensitive isotope proxies and OC (abundances, isotope ratios) that together could unveil a more complete perspective of C cycling during soil formation.

In this study, we explore connections between clay mineral formation and OC accumulation in fluvial systems, resolving a previously unknown connection between the inorganic and organic carbon cycles. We compile previously published measurements of soil from Hawaii (Torn et al., 1997; Ryu et al., 2014; Huh et al., 2004; Li et al., 2020) and measure Li isotope ratios of river suspended sediment from two watersheds with different climatic and geologic conditions. We show how these measurements, when compared to a coupled model of OC cycling and silicate weathering, can refine the controls and coupling of silicate weathering and OC cycling. The results underscore bedrock chemistry and reaction stoichiometry as a mutually fundamental control of weathering and OC cycling.

2. Description of study area

The three study sites encompass a range of climatic, geologic, and lithologic conditions. The first are the well-characterized Hawaii chronosequence (Torn et al., 1997; Ryu et al., 2014) and climosequence (Huh et al., 2004; Li et al., 2020) soils. Whereas the chronosequence contains ridgetop soils from 0.3 to 4,100 kyr in age which together have been interpreted as a classic example of soil development over time (Chadwick et al., 1999), the climosequence soils are comparable in age but form across a range of climatic conditions and ecological zones. All soils form from the weathering of basalt and dust and contain variable amounts of amorphous phases, like allophone and imogilite, and crystalline phases, like kaolinite and gibbsite. Amorphous phases are most abundant in soil $\leq$ 150 kyr old and are replaced by crystalline ones as soils age (Chadwick et al., 1999; Torn et al., 1997). We focus on soil profiles that develop in highly productive rainforest-like climates and

are not heavily impacted by aerosol input (see Supporting Information and Figs. S1–S3 for further justification). Fossil pollen grains show that climate has changed over the time encompassed by the chronosequence and climosequences, but studies argue that climate change minimally impacted the trajectory of soil formation (Hotchkiss et al., 2000). All data from Hawaii presented here considers whole-soil average OC content (Torn et al., 1997) and Li-weighted average δ^7Li values (where $\delta^7\text{Li}_{unknown} = [\frac{^7\text{Li}}{^6\text{Li}_{unknown}} / \frac{^7\text{Li}}{^6\text{Li}_{\text{LSVEC}}}] - 1$) (Ryu et al., 2014) for each soil profile.

The additional two sites where we generate new datasets are the Little Deschutes River in the eastern Cascade Range of Oregon, USA and the Rio Bermejo in Argentina and Bolivia (Fig. S4). The Little Deschutes River was recently deglaciated after Last Glacial Maximum, contains exclusively volcanic bedrock (pumiceous ash from the 7 kya eruption of Mt. Mazama, rhyodacites, Quaternary basalt flows), and is mostly pristine, having been designated by the US Forest Service as protected wilderness in 1984 (Gannett, 2004). We focus on the headwaters of the Little Deschutes River that flow proximally to bedrock sources (Fig. S5). With negligible petrogenic OC and bedrock phyllosilicates, the watershed and the chemistry of its soil and river sediment are interpreted as chiefly the byproduct of near-surface biogeochemical cycling (Dudas and Harward, 1975). Amorphous phases like halloysite, allophane, and ferrihydrite are the dominant byproducts of weathering in the watershed (Dudas and Harward, 1975). The climate in the watershed is temperate where wintertime snowfall is the primary form of precipitation and snowmelt drives discharge in late spring.

The Rio Bermejo is a larger drainage than the Little Deschutes, and it flows eastward from the central Andes into the continental interior without any tributaries for over 1000 km of flow (Repasch et al., 2023). The mean residence time of sediment in the lowland floodplain is approximately 8.4 kyr (Repasch et al., 2020). The fluvial environment is thought to be at a steady state with respect to aggradation rates in the foreland basin and rates of uplift in the adjoining Andes (Repasch et al., 2021). Recycled sedimentary rocks that contain petrogenic OC (0.01–0.04 wt.%) and primary phyllosilicates compose the bedrock in this watershed (McGlue et al., 2016; Scheingross et al., 2021), which is characteristic of Andean foreland basins (Dellinger et al., 2014). Smectite and illite are the main secondary clay minerals that form during weathering (McGlue et al., 2016). Climate in the watershed is subtropical with monsoonal precipitation controlling river discharge (Repasch et al., 2021).

Unlike the Hawaii soil profiles, our study of the Rio Bermejo and Little Deschutes involves the analysis of river suspended sediment. The composition of river suspended sediment typically reflects catchment-wide silicate weathering, sediment provenance, and clay formation (Lupker et al., 2012; Malkowski et al., 2019), potentially offering a different and complementary perspective on biogeochemical cycles at the watershed scale. For the Little Deschutes River, we analyze bedrock and river suspended sediment for Li isotope ratios and element concentrations and soil and suspended sediment for OC concentrations, stable C isotopes, and radiocarbon content (see Methods). For the Rio Bermejo, since measurements of OC and of sediment/soil properties were conducted in previous studies (Repasch et al., 2020, 2021; Scheingross et al., 2021), we solely analyze river suspended sediment for Li isotope ratios and element concentrations.

3. Methods

3.1. Data compilation and calculations for Hawaii soils

All soil profile measurements from Hawaii were compiled from previous studies (Huh et al., 2004; Li et al., 2020; Mikutta et al., 2009; Ryu et al., 2014; Torn et al., 1997) and used to quantify soil-average compositions (Eqs. (1) and (2)). Each study reports sample localities, bedrock ages, and depths that sample was retrieved. Each chronosequence study (Mikutta et al., 2009; Ryu et al., 2014; Torn et al., 1997) sampled soil from an individual profile, and we assume that each soil profile is representative of soil formation processes at a given locality. For a given soil quantity $\mathcal{J}$, we compute depth-integrated values using the trapezoidal rule such that

$$\mathcal{J}_{average} = \frac{1}{z_{bot} - z_{top}} \int_{z_{top}}^{z_{bot}} \mathcal{J}(z)\, dz \approx \frac{1}{z_{bot} - z_{top}} \cdot \frac{1}{2}\left(\mathcal{J}_1 \Delta z_1 + 2 * \mathcal{J}_2 \Delta z_2 + \cdots + 2 * \mathcal{J}_{N-1} \Delta z_{N-1} + \mathcal{J}_N \Delta z_N\right) \quad (1)$$

where z_{bot} is the bottom of the soil profile, z_{top} is the top of the soil profile, $z_{bot} - z_{top}$ is the length of the soil profile, $\mathcal{J}_i$ is a quantity of sample i from a given soil profile, Δz_i is the depth interval of sample i, and N is the total number of samples in a soil profile.

One study (Mikutta et al., 2009) designates the depth of soil B horizons for each locality and reports soil properties and reactive element concentrations that are helpful to compare with Li isotope ratios. In instances where we compute depth-integrated averages of entire soil profiles, we let $z_{top} = 0$ where 0 corresponds to the top surface of the soil. When computing depth-integrated averages of B horizons, we let $z_{top} = z_B$ where z_B is the top of the B horizon.

For Li isotope ratios, we compute Li-weighted averages values (also using the trapezoidal rule) where

$$\delta^7\text{Li}_{soil,average} = \frac{\int_{z_{top}}^{z_{bot}} \text{Li}(z)\, \delta^7\text{Li}(z)\, dz}{\int_{z_{top}}^{z_{bot}} \text{Li}(z)\, dz} \quad (2)$$

and Li(z) and δ^7Li(z) are the depth profiles of Li concentrations and Li isotope ratios, respectively.

3.2. Sample acquisition, preparation, and analysis for the Rio Bermejo and Little Deschutes river

For the Rio Bermejo, the sampling protocol for river suspended sediment and details for stable C and radiocarbon analyses can be found in previous studies (Repasch et al., 2020, 2021; Scheingross et al., 2021).

All samples from the Little Deschutes River, Oregon, USA were collected over two field seasons spanning August 2021 and June 2022. Exposed bedrock that lacked obvious evidence of weathering product was gathered with a hammer and chisel and stored in new Ziploc® bags. Soil was retrieved with an auger, collected at regular depth intervals (5–10 cm), stored in new Ziploc® or WhirlPak® bags, and placed in a freezer (−4 °C). For each river suspended sediment sample, 30–50 L of river water was collected with a Van Dorn sampler ~1 m below the water surface near the river thalweg, and subsequently stored in new, 10 L polyethylene bags (Smart Bottles Inc.). The water was then filtered through polyethersulfone filters using a plastic filter holder and a manually operated pump to isolate sediment (> 0.22 μm fraction). All sediment-laden filters were stored in a freezer (−4 °C).

At the time of analysis, soil and sediment-laden filters were dried in an oven at 50 °C. Once dry, soil was gently dis-aggregated and sieved to remove coarse sediment (> 2 mm) and then split into aliquots with a riffle splitter. All visible macrophytes were handpicked from the sediment-laden filter and the remaining sediment was removed by gently squirting doubly deionized water (18.2 MΩ) onto the sediment surface. The sediment-water slurry was collected in pre-combusted glass scintillation vials and evaporated to dryness in an oven at 50 °C. The sediment was homogenized with a Teflon spatula. Bedrock was cut with a water saw with care taken to remove any pieces that had evidence of weathering (e.g., oxide deposits). A ~2 cm^3 piece of bedrock was then powdered with a clean tungsten carbide ball mill.

Aliquots of soil and sediment were used for a series of chemical analyses: element concentrations, Li isotope ratios, bulk OC content, stable C isotope ratios, and radiocarbon content. Aliquots of bedrock powders

only underwent analyses for element concentrations and Li isotope ratios. Prior to element and Li isotope analyses, approximately 10 mg of sample was weighed, digested in a series of ultrahigh purity acids (PlasmaPURE Plus grade HF, HNO_3, and HCl from SCP Science), and reconstituted in 6N HNO_3. An aliquot of sample digest (5% v/v) was dedicated for major and trace element analyses and the remaining digest (95% v/v) was used for Li isotope ratios. All major, minor, trace, and rare earth element analyses were conducted on a Thermo iCAP triple quadrupole ICP-MS equipped with a dual direct-injection system at Rice University. The major/trace element sample aliquots were diluted ~8,000× in 1% (v/v) HNO_3 and introduced in solution into the instrument. The dual direct-injection system enabled the simultaneous uptake of sample and an in-house standard (2 ppb In, Sc, and Y solution), permitting the detection and correction of instrument drift during each analytical session. Calibrations for each element were performed using external gravimetric solutions, and blanks and external reference standards were analyzed every ~12 samples. Error on reference materials was <10%.

All preparation and measurement of Li isotope ratios were conducted at the University of Texas at Austin. Prior to measurement, the remaining aliquots of sample digest were evaporated to dryness in Teflon beakers and reconstituted in 0.67N HNO_3 + methanol (30% v/v) for 24 hours. Li purification via column chromatography followed (Ramos et al., 2022) with at least one reference standard (IAPSO standard seawater or JR-1 rhyolite) analyzed per session of column chromatography. All isotope ratios were analyzed on a Nu Plasma 3D Multicollector ICP-MS with IRMM-16 serving as the bracketing standard between each measurement of an unknown. To calculate a δ^7Li value, all unknown ^{7}Li/^{6}Li ratios were normalized by the average ^{7}Li/^{6}Li ratio of its corresponding bracketing standards and reported relative to lithium carbonate 8545-LSVEC. The long-term average measured δ^7Li_{JR-1} value = 4.03 ± 0.47‰ (2 s.d.; n = 21; accepted δ^7Li_{JR-1} value = 4 ± 0.3‰; Qi et al., 1997) and the long-term average measured δ^7Li_{IAPSO} value = 31.29 ± 0.76‰ (2 s.d.; n = 43; accepted δ^7Li_{IAPSO} value = 30.88 ± 0.12‰; Huang et al., 2010).

Bulk organic C and N concentrations of suspended sediment (~ 1–10 mg of sediment) were measured at Rice University using a Costech Instruments Elemental Analyzer and C concentrations of bulk soil (~ 1–10 mg of soil) were measured at Brown University using a Delta V Plus GC-EA-IRMS. Replicate analyses of international standard materials (e.g., PACS-3 from Environment Canada) every 10–12 samples were measured to assess accuracy and precision. All stable C and radiocarbon analyses were conducted at the National Ocean Sciences Accelerator Mass Spectrometry Facility (NOSAMS) with the former using an elemental analyzer-isotope ratio mass spectrometer and the latter using an accelerator mass spectrometer. All radiocarbon data are converted to a fraction modern carbon (Fm. C) by calculating the difference between the sample ^{14}C activity and 95% the ^{14}C activity of NBS Oxalic Acid I (SRM 4990B, OX-I) normalized to $\delta^{13}C_{VPDB}$ = -19‰. For fraction modern calculations, isotopic fractionation is corrected using the measured ^{13}C/^{12}C to the value of δ^{13}C = -25‰.

3.3. OC cycling and weathering model

A set of ordinary differential equations (ODEs) are derived below to capture the coupled evolution of OC cycling, mineral dissolution and formation, and Li isotope transfer. To limit the number of parameters for OC cycling and weathering reactions, we simplify constitutive mass transfer equations by assuming soil as a uniform box but include sufficient detail so that measured Li isotope ratios and OC contents can be linked to first-order soil formation processes. Operationally, the effect of OC oxidation on mineral dissolution and formation can be toggled on or off in these ODEs, which we use to ascertain the directional effects of OC cycling on silicate weathering reactions. We define two C pools that broadly represent particulate OC (a fast cycling pool denoted as OC_{fast}) and mineral-associated OC (a slow cycling pool denoted as OC_{slow}), bedrock (subscript $rock$), clay (subscript $clay$), and water (subscript $water$) as constituents of soil. The transfer of OC is described as

$$\frac{dOC_{fast}}{dt} = P_{C_{fast}} - k_{C_{fast}} OC_{fast} \tag{3}$$

and

$$\frac{dOC_{slow}}{dt} = f_{C_{trans}} k_{C_{fast}} OC_{fast} - k_{C_{slow}} OC_{slow} \left(\frac{X_{rock_i}}{X_{clay}}\right)^n \tag{4}$$

where OC_{fast} [M·L^{-3}] is driven by gross primary productivity per depth of soil $P_{C_{fast}}$ [M·L^{-3}·T^{-1}] and its intrinsic transformation rate $k_{C_{fast}}$ [T^{-1}], and OC_{slow} is driven by inputs from OC_{fast} transformation and outputs from its transformation. Of the OC_{fast} that is transformed, only a fraction $f_{C_{trans}}$ [M·M^{-1}] of that transformation yields C_{slow} accumulation with the remaining fraction (1-$f_{C_{trans}}$) either available as dissolved organic carbon (DOC) or dissolved inorganic carbon (DIC) for mineral dissolution (f_{diss,C_f}) or exported (1-f_{diss,C_f}). The transformation of OC_{slow} is a nonlinear function of the relative mass abundance of initial bedrock X_{rock_i} [M·L^{-3}] and secondary clay X_{clay} [M·L^{-3}], modified by the positive exponent n [unitless]. In this formulation, higher clay abundances suppress the transformation of OC_{slow}.

The dissolution of bedrock X_{rock} is described as

$$\frac{dX_{rock}}{dt} = -\mathcal{K}_{rock} X_{rock} \tag{5}$$

where $\mathcal{K}_{rock}$ is the effective rock dissolution rate [T^{-1}] that is the sum of intrinsic dissolution rate k_{rock} and the organic-enhanced dissolution rate (Lawrence et al., 2014), expressed in its complete form as

$$\mathcal{K}_{rock} = (1 - f_{C_{trans}}) f_{diss,C_f} k_{C_{fast}} M_{fast} a_{rock} \beta + \cdots$$
$$f_{diss,C_s} k_{C_{slow}} \left(\frac{X_{rock_i}}{X_{clay}}\right)^n M_{slow} a_{rock} \beta + k_{rock}. \tag{6}$$

In this formulation, we also assume that a remaining fraction of transformed OC_{slow}, f_{diss,C_s}, is available for silicate weathering and that the proportion of DIC/DOC that reacts with bedrock versus clay is a function of the relative mass abundance of OC M (akin to an activity) and mass-weighted relative surface area of bedrock or clay a. For example, M_{slow} and a_{rock} are expressed as

$$M_{slow} = \frac{OC_{slow}}{X_{rock} + X_{clay}} \tag{7}$$

and

$$a_{rock} = \frac{A_{rock} X_{rock}}{A_{rock} X_{rock} + A_{clay} X_{clay}} \tag{8}$$

where

$$a_{rock} + a_{clay} = 1. \tag{9}$$

A [L^2·M^{-1}] is the specific surface area of a corresponding phase. We assume A_{rock} to have a specific surface area of plagioclase and A_{clay} to have a specific surface area of kaolinite. We lastly modify the fast and slow OC-enhanced dissolution terms by a splitting fraction β [M·M^{-1}] that tempers the effect of DIC/DOC activity on dissolution rates, qualitatively similar to treatments in previous studies (Drever, 1994; Lawrence et al., 2014).

Like X_{rock}, clay content X_{clay} can be expressed as

$$\frac{dX_{clay}}{dt} = f_{clay} \mathcal{K}_{rock} X_{rock} - \mathcal{K}_{clay} X_{clay} \tag{10}$$

where clay formation is proportionate to bedrock dissolution, scaled by fraction f_{clay} [M·M^{-1}], and its dissolution rates $\mathcal{K}_{clay}$, which is the sum of its intrinsic dissolution rate k_{clay} and organic-enhanced dissolution:

$$\mathcal{K}_{clay} = (1 - f_{C_{trans}}) f_{diss,C_f} k_{C_{fast}} M_{fast} a_{clay} \beta + \cdots$$

$$f_{diss,C_s} k_{C_{slow}} \left(\frac{X_{rock_i}}{X_{clay}}\right)^n M_{slow} a_{clay} \beta + k_{clay}. \quad (11)$$

In the absence of organic-enhanced dissolution, Eqs. (6) and (11) simply become $\mathcal{K}_{rock} = k_{rock}$ and $\mathcal{K}_{clay} = k_{clay}$, respectively. With Eqs. (3)–(11), we derive equations for the conservation of Li and its isotopes. In treating soil as a batch reactor, we can assume a coexisting fluid phase (liquid water) that mediates weathering reactions and neither flows into or out of the domain. The Li content and isotope composition of water will be a function of the relative amount of mineral dissolution to clay formation (Bouchez et al., 2013; Dellinger et al., 2015), which can be described as

$$\frac{d\mathrm{Li}_{water}}{dt} = \frac{1}{\rho_{water}}\left[\mathcal{K}_{rock} X_{rock}(\mathrm{Li}_{rock} - f_{clay} D_{\mathrm{Li}} \mathrm{Li}_{water}) + \mathcal{K}_{clay} X_{clay} \mathrm{Li}_{clay}\right] \quad (12)$$

where Li is the Li concentration [M·M^{-1}], D_{Li} [M·M^{-1}] is the partition coefficient of Li between secondary clay and water, and ρ_{water} [M·L^{-3}] is the density of water. This model assumes that all newly formed clay minerals incorporate Li from solution and that bedrock Li content is a constant. As a result, clay Li content evolves over time and is expressed as

$$\frac{d\mathrm{Li}_{clay}}{dt} = f_{clay} \mathcal{K}_{rock} \frac{X_{rock}}{X_{clay}} \left(D_{\mathrm{Li}} \mathrm{Li}_{water} - \mathrm{Li}_{clay}\right). \quad (13)$$

With the Li content of secondary clay and water considered, $\delta^7\mathrm{Li}_{water}$ values can be expressed as

$$\frac{d\delta^7\mathrm{Li}_{water}}{dt} = \frac{1}{\rho_{water}\mathrm{Li}_{water}} \times \cdots \left[\mathcal{K}_{rock} X_{rock} \mathrm{Li}_{rock}(\delta^7\mathrm{Li}_{rock} - \delta^7\mathrm{Li}_{water}) + \cdots \mathcal{K}_{clay} X_{clay} \mathrm{Li}_{clay} \Delta_{clay} - \cdots f_{clay} \mathcal{K}_{rock} X_{rock} D_{\mathrm{Li}} \mathrm{Li}_{water} \Delta_{clay}\right] \quad (14)$$

where all isotope fractionation between secondary clay and water follows equilibrium, temperature-dependent batch fractionation (Bouchez et al., 2013) such that

$$\Delta_{clay} = 1000 \log \alpha_{clay-water}(T) \approx \delta^7\mathrm{Li}_{clay} - \delta^7\mathrm{Li}_{water}. \quad (15)$$

In the simulations, we assume a constant Δ_{clay} value when computing $\delta^7\mathrm{Li}_{clay}$ values from $\delta^7\mathrm{Li}_{water}$ values. Mineral dissolution is assumed not to fractionate Li isotopes, although solution pH has a subtle impact on the magnitude of isotopic fractionation during dissolution (Zhu et al., 2023).

Altogether, bulk soil Li concentrations and δ^7Li values can be calculated whereby

$$\mathrm{Li}_{soil} = \frac{X_{rock}\mathrm{Li}_{rock} + X_{clay}\mathrm{Li}_{clay}}{X_{rock} + X_{clay}} \quad (16)$$

and

$$\delta^7\mathrm{Li}_{soil} = \frac{X_{rock}\mathrm{Li}_{rock}\delta^7\mathrm{Li}_{rock} + X_{clay}\mathrm{Li}_{clay}\delta^7\mathrm{Li}_{clay}}{X_{rock}\mathrm{Li}_{rock} + X_{clay}\mathrm{Li}_{clay}}. \quad (17)$$

4. Results

4.1. Geochemical data

All geochemical data can be found in the Supporting Information. The δ^7Li values of river suspended sediment in the Rio Bermejo span −2.6 to +4.1‰ (n = 13) whereas those in the Little Deschutes span −10.1 to −2.0‰ (n = 23). Of the samples whose bedrock sources are well characterized and have paired OC concentrations in the Little Deschutes (see Fig. S5), the range of δ^7Li values narrows from −10.1 to −5.2‰ (n = 14). The Li-weighted average soil δ^7Li values from Hawaii span −0.1 to 5.6‰ (n = 8). The range of sediment/soil OC contents for Rio Bermejo, Little Deschutes, and Hawaii are 0.1 to 0.4 wt.%, 7.9 to 17.6 wt.%, and 2.2 to 15.4 wt.%, respectively. River sediment and soil OC content from Rio Bermejo compare well, whereas the range of river sediment OC content generally exceeds soil OC contents for Little Deschutes, albeit with some overlap (Fig. S6). For bedrock source δ^7Li values, we assume a bedrock composition of +4.1 ± 0.5‰ for the Rio Bermejo, which is the highest measured value from our river sediment samples and comes from the sample with the highest fraction sand. We measure a range of values in the Little Deschutes from −3.1 to +7.4‰ (n = 9) and use its mean value (+3.3‰) since the sediment provenance and spatial distribution of bedrock δ^7Li values lack distinctive trends (Fig. S5). Lastly, we use an average of the reported values for lava flows and Asian dust sources, approximately equal to +4.0‰ (Huh et al., 2004; Li et al., 2020). We take the difference between $\delta^7\mathrm{Li}_{fine}$ ("fine" meaning soil or river suspended sediment) and their locality-specific mean or assumed $\delta^7\mathrm{Li}_{rock}$ value to constrain weathering signals where $\Delta^7\mathrm{Li}_{fine-rock} = \delta^7\mathrm{Li}_{fine} - \delta^7\mathrm{Li}_{rock}$ (Dellinger et al., 2017).

When arrays of Li isotope ratio differences and OC contents are fit with a Deming regression, we find statistically significant negative correlations (Fig. 2). The Hawaii and Little Deschutes arrays have comparably steep slopes in OC-δ^7Li space whereas the slope of the Rio Bermejo array is notably shallow. For each array, the lowest $\Delta^7\mathrm{Li}_{fine-rock}$ values,

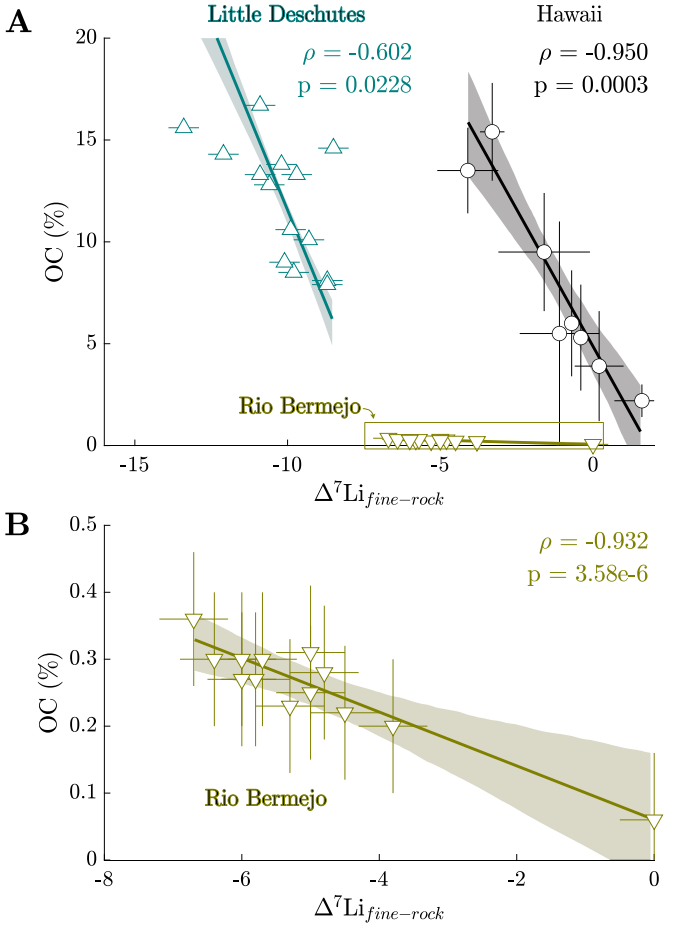

Fig. 2. Li isotope and OC data for each study site. A) OC content versus δ^7Li difference between "fine" (suspended sediment or bulk soil) and bedrock. B) Li isotope and OC array for the Rio Bermejo array (inset of A). Listed beside each array are p values and Spearman's rho. Hawaii data correspond to bulk soil average values (error bars are standard errors) whereas Rio Bermejo and Little Deschutes are measurements of river suspended sediment. Their error bars correspond to long-term precision (2σ) of replicate standards (0.5‰ for δ^7Li values and 0.1% for OC abundances). All arrays contain 1σ error envelopes (68% confidence).

often interpreted as representing the most intense silicate weathering (Dellinger et al., 2017; Winnick et al., 2022), are associated with the highest OC contents. Li isotope ratios of Rio Bermejo sediment and Hawaii soil correlate with reactive Mn, Fe, and Al content, stable C isotope compositions, and grain size (Fig. S7–S8), where lower δ^7Li values correspond to high relative abundances of reactive elements as well as low sand fractions. Li isotope ratios of Little Deschutes sediment do not correlate with bulk stable C isotopes (Fig. S9). In both watersheds and Hawaii, the Li isotope ratios do not correlate with radiocarbon content, although Li isotopes and radiocarbon exhibit some spatial and/or temporal trends (Fig. S10–S12). The role of fluvial mixing in the Rio Bermejo and Little Deschutes (Fig. S12) might explain these weak correlations. Together, these results show consistent interactions of the organic and inorganic components of the C cycle. Yet, the varying absolute ranges of Li isotope ratios and OC contents among the localities may indicate differing environmental modulators of OC burial and/or silicate weathering, or differences in analyzed material (i.e., soil vs. river suspended sediment).

4.2. Model predictions

To understand processes that underlie these OC-Li isotope arrays (Fig. 2), we model expressions of mass transfer linking the turnover of OC with the formation and dissolution of silicates (see Supporting Information for details on non-dimensionalization). Given our treatment of soil as a single reservoir, we interpret compositional changes as representing average, watershed-scale biogeochemical cycling (Bouchez et al., 2013).

Assuming that an initial soil reservoir contains solely bedrock, the change of clay Li isotope ratios and OC abundances over time follows a consistent path (Fig. 3, 4). As bedrock dissolves and clays precipitate from solution, clays reduce the transformation rate of OC_{slow} (Eq. (4)), enabling this OC pool to grow. OC_{fast}, insensitive to clay formation, rapidly reaches a steady state due to its high transformation rate. Clays also incorporate aqueous Li when they form and cause δ^7Li_{water} values to increase. The increase in Li concentrations in water and newly formed clay at early time show that the supply of Li from bedrock dissolution exceeds uptake of Li by clay during formation, and the plateauing of Li concentrations and δ^7Li_{water} values at later time reflect the balance of Li inputs to and outputs from solution (Fig. 3A). Clay δ^7Li values, assuming equilibrium batch fractionation (Eq. (15)), will mirror this trend and steadily increase in value from more negative ones over time (Fig. 3B). The value of Δ_{clay} (Eq. (15)) impacts the absolute range $\Delta^7Li_{clay-rock}$ values most at early time (Fig. S13) but becomes less noticeable as time proceeds.

OC-enhanced dissolution rates can have a sizable impact on both OC and weathering dynamics (Fig. 3, 4). In models with low OC-enhanced weathering ($f_{diss,C_f} = f_{diss,C_s} = 0$; Eqs. (6) and (11)), where either OC inputs as gross primary productivity are low or export of transformed OC is high, the turnover of bedrock, clay, and OC_{slow} occurs over a longer time span than in high OC-enhanced weathering models ($f_{diss,C_f} = f_{diss,C_s} = 1$; Fig. 3A, 4). The resultant low bedrock and clay dissolution rates also enable greater accrual of OC_{slow} given the longer time span of clay accumulation. Soil development during high OC-enhanced weathering models advances more quickly because of increased mineral dissolution and formation rates (Figs. 3A, 4D). The high specific surface areas of clays (Table S1) make them especially prone to OC-enhanced dissolution (Bouchez et al., 2013; Drever, 1994). Thus, the amount of clay will decrease once the cumulative amount of clay surfaces exceeds those of bedrock mineral surfaces (Eq. (8); Fig. 3A) and become primary targets of transformed OC. In contrast, clay abundances decrease in low OC-enhanced weathering models only when bedrock minerals have completely weathered away (Ferrier and Kirchner, 2008). Both models show that clay dissolution causes δ^7Li_{water} values to decrease and water Li concentrations to increase as more clay-bound Li is introduced in solution, bulk δ^7Li_{soil} values to begin decreasing (Fig. 5)

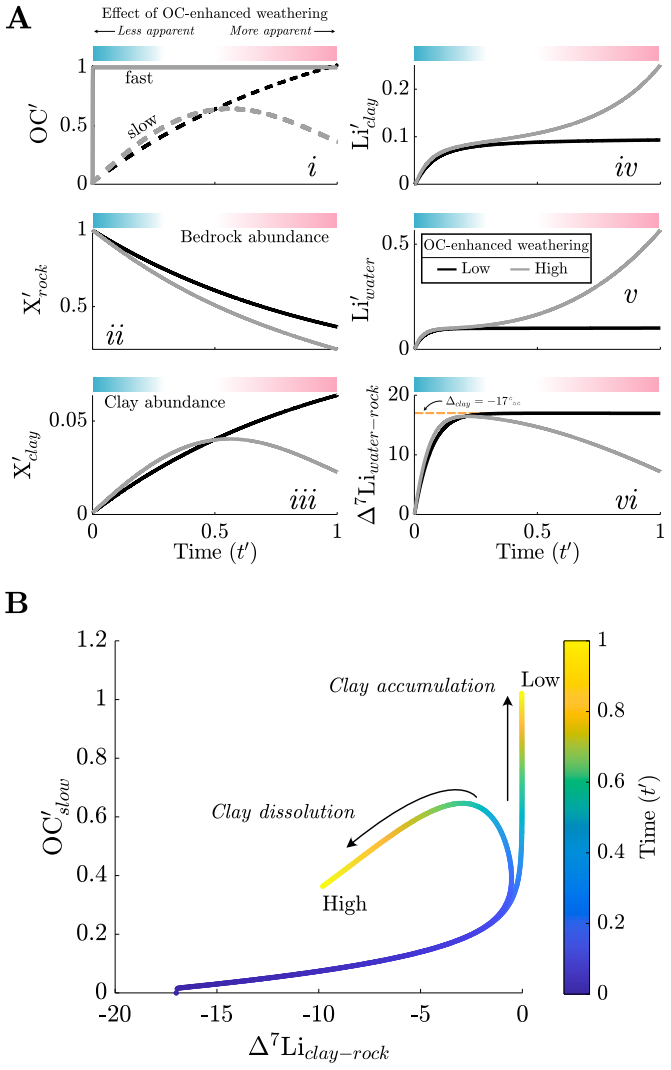

Fig. 3. Example model predictions with low (black lines) and high (gray lines) OC-enhanced dissolution. Note that all variables are non-dimensionalized (denoted with primes; see Supporting Information) to better convey relative differences between simulations. A) Temporal trajectories of fast OC (solid lines) and slow OC (dashed lines) (panel *i*), bedrock (X_{rock}; panel *ii*) and clay abundances (X_{clay}; panel *iii*), clay and water Li concentrations (panels *iv* and *v*), and water δ^7Li values relative to bedrock (panel *vi*). The imposed per-mil fractionation factor between clay and water ($\Delta_{clay} = -17$‰) is delineated with a dashed line. Bedrock δ^7Li values are constant across model time (δ^7Li_{rock} = 3‰). Note that the model trajectories depart from one another significantly at intermediate time ($t' \approx 0.4$–0.5) once clay minerals achieve modest abundances; this is emphasized with a color bar where it indicates the less and more apparent effects of OC-enhanced dissolution on model outcomes. B) Model predictions for slow OC accumulation and clay δ^7Li values (calculated with δ^7Li_{water} and Δ_{clay} following Equation (15)) at high and low OC-enhanced weathering scenarios. The sole difference between model scenarios are the values of f_{diss,C_f} and f_{diss,C_s}, where $f_{diss,C_f} = f_{diss,C_s} = 1$ for high OC-enhancement and values $f_{diss,C_f} = f_{diss,C_s} = 0$ for low OC-enhancement.

(Bouchez et al., 2013), and OC_{slow} abundances to decrease proportionate to clay decreases. The consistent evolution of soil compositions in both model scenarios shows that OC-enhanced dissolution primarily acts to accelerate soil development rather than change its overall pathway of development. As a result, the timescales of observations and/or watershed longevity may limit the ability to corroborate the role of OC-enhanced dissolution in natural systems and thus evaluate this possible linkage between OC cycling and silicate weathering.

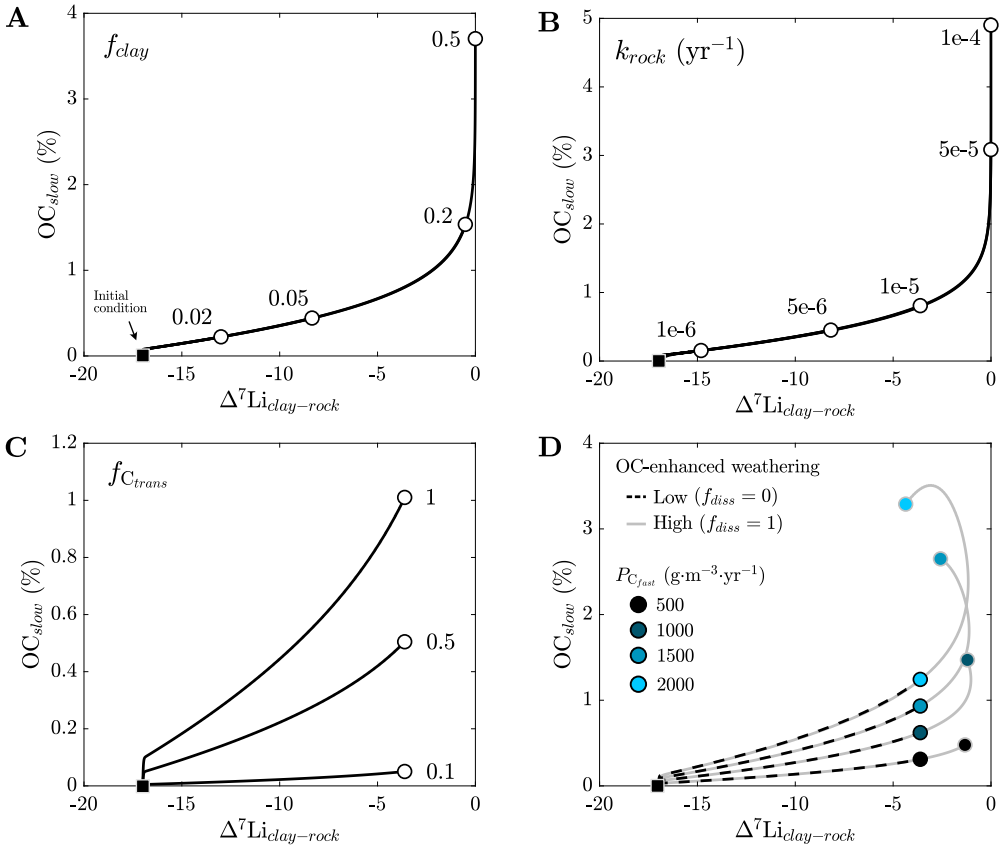

Fig. 4. Model sensitivity analyses of fractional clay formation f_{clay} (panel A), intrinsic rock dissolution rates k_{rock} (panel B), OC_{fast} fraction converted to OC_{slow} $f_{C_{trans}}$ (panel C), and primary productivity $P_{C_{fast}}$ (panel D) at high and low OC-enhanced dissolution f_{diss}. For each sensitivity analysis, the sole difference among the simulations are the variables listed. The lines correspond to the pathway of OC_{slow} and δ^7Li_{clay} change over a given model time and the circles are the end times. Time zero for all models is at $OC_{slow} = 0$ and $\Delta^7Li_{clay-rock} = -17‰$ (black square). The value of the corresponding parameter value (in panels A-C) is listed beside the model trajectory endpoints. For f_{clay} and k_{rock}, note the similar pathways of change, where increase f_{clay} and k_{rock} yield increase distances along the pathway. Note also that $f_{C_{trans}}$ has no fundamental impact on Li isotope ratios. Lastly, note that for high and low OC-enhanced dissolution simulations (panel D), there are similar pathways that the simulations follow. OC_{slow} increases with increasing $P_{C_{fast}}$, but high organic acid generation enables more OC_{slow} to accrue. The decrease in OC_{slow} and δ^7Li_{clay} values at later time, most apparent at high $P_{C_{fast}}$, is the result of the onset of clay mineral dissolution. We let $f_{diss,C_f} = f_{diss,C_s}$ in these simulations.

5. Discussion

5.1. Fluvial mixing vs. heterogeneous biogeochemical cycling across landscapes

This model exercise crucially illustrates that over a range of parameter values that agree with the geologic and environmental conditions of the three study sites (Fig. 4, S13), OC_{slow} and $\Delta^7Li_{clay-rock}$ values will always increase at early time, forming a positive slope in OC-Li isotope space (Fig. 3). A negative slope in this space could only be achieved if rates of secondary clay turnover far exceed bedrock dissolution, which could be the case for old, well-developed soils with pronounced horizonation. It is furthermore unclear how fluid flow (absent from models) would simultaneously promote clay turnover and suppress bedrock dissolution. Therefore, the negative correlations observed at each locality (Fig. 2) do not simply represent a temporal evolution of soil development and instead involve other modulators. We consider two likely, and not mutually exclusive, explanations that may bridge model findings with observations: 1) that suspended sediment contain a mixture of newly formed clay minerals and bedrock fragments and 2) that rates of weathering and OC cycling differ across a watershed.

Watersheds, with internally heterogeneous physiography, contain sediment that experience a wide extent of weathering conditions, rates of OC turnover, and residence times. The transit of sediment across landscapes in rivers involves the erosion, suspension, and re-deposition of sediment that may buffer *in situ* biogeochemical signals (Straub et al., 2020). River suspended sediment thus encodes variable histories of watershed evolution, reducing the likelihood that their chemistry should directly follow one idealized soil formation pathway (Fig. 3B). At one simplified extreme, we can assume that weathering across a watershed is occurring uniformly in rate and duration and that the river sediment is a simple binary mixture of newly formed clay minerals and un-weathered bedrock fragments (Fig. 6A). The resultant mixing arrays indeed generate negative, monotonic relationships between OC_{slow} and δ^7Li_{clay} values, albeit highly nonlinear relationships at early time. The nonlinearity results from an uneven distribution of Li between new clay minerals and bedrock where, in this case, bedrock Li concentrations far exceed clay Li concentrations at early time (see SI for mixing calculations). An increase in Li partition coefficients between clay and water will yield more linearity in the mixing arrays at early time, but this change will also modify how quickly δ^7Li_{clay} values increase as time elapses. Moreover, the inclusion of old authigenic clay as a possible sediment source, along with newly formed clay and bedrock fragments, could yield an array of slopes in OC-δ^7Li space. The relationships between δ^7Li_{fine} and suspended sediment concentration in the Little Deschutes and Rio Bermejo (Fig. S12) support that fluvial mixing between multiple clay endmembers is at least partially responsible for OC-Li isotope trends. Altogether, the dilemmas that can arise from such parameter modifications or endmember selections highlight the challenge of ascribing mixing to these data trends.

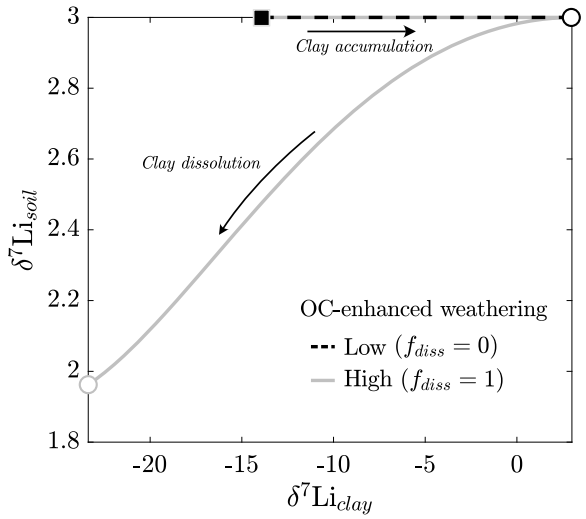

Fig. 5. Model trajectories of Li isotope ratios of clay and bulk soil in two model scenarios: one with no OC-enhanced dissolution and one with the maximum amount of OC-enhanced dissolution (same simulations as in Fig. 3). All parameters except f_{diss} (we let $f_{diss,C_f} = f_{diss,C_s}$) are identical between each model run. Each model is run for the same length of time where the line corresponds to the model pathway and the circle corresponds to values at the end time. Note that there can be wide fluctuations in clay δ^7Li values with little change in soil δ^7Li because little amounts of clay have been generated. The high OC-enhanced dissolution model shows a modest decrease in clay and soil δ^7Li at later time as primary bedrock has been exhausted and any clay left in the profile are predominantly undergoing dissolution.

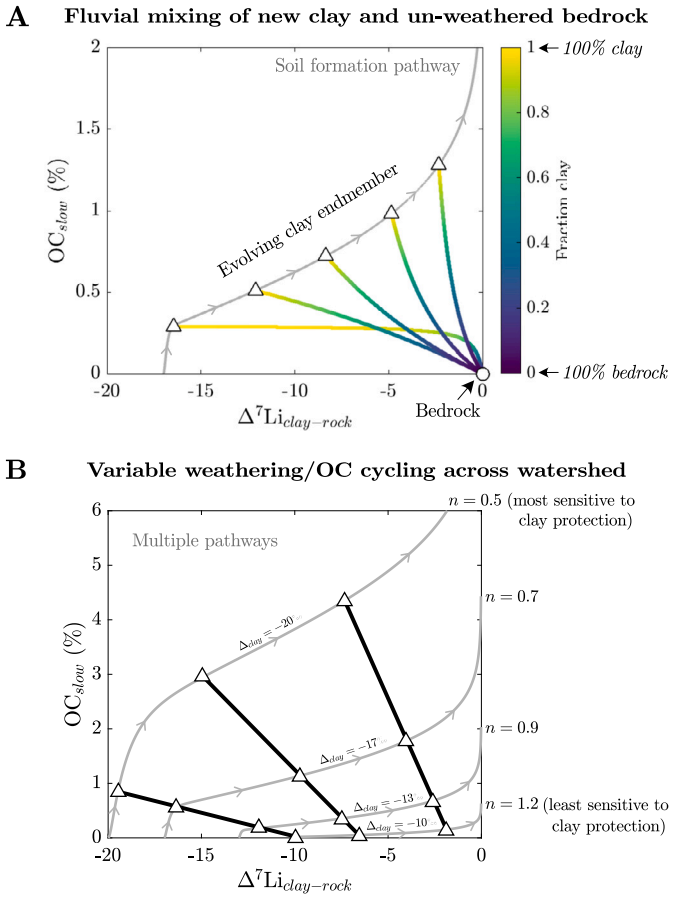

Fig. 6. Example simulations and calculations that showcase how fluvial mixing or OC sensitivity to clay protection can underlie OC-Li isotope arrays. A) Predicted OC_{slow} content and $\Delta^7Li_{clay-rock}$ values in a scenario where newly formed clay (triangles) at different times along a closed-system soil formation pathway (gray line; like those in Fig. 3B) mix with bedrock. Each array corresponds to theoretical mixing between clay forming at different timesalong the pathway. The nonlinearity is the result of Li concentration differences between clay and bedrock. B) Model predictions with varying OC sensitivity to clay protection n. Multiple pathways are shown that also have differing fractionation factors Δ_{clay}, and black lines show hypothetical negative arrays if multiple soil formation pathways for each sediment are inferred. A decrease in n indicates a higher sensitivity of clay formation to OC protection. Note that decreases in $k_{C_{slow}}$ (i.e., more sluggish rates of OC_{slow} transformation) or increases in $P_{C_{fast}}$ (i.e., larger inputs of OC to soil) can accomplish a similar change in model sensitivity as a decrease in n.

At another extreme, we can consider river sediment as a mixture of sediment grains each with its own history of weathering and OC cycling (Fig. 6B). To generate a wide span of δ^7Li_{clay} values at given locality, mineral dissolution rates, clay formation rates, and/or the duration of soil formation must vary (Fig. 4). The occurrence of low δ^7Li_{clay} values at both high or low weathering rates/durations (Figs. 3B, 4D) complicates the interpretation of Li isotope ratios. However, for fluvial environments like the Rio Bermejo and Little Deschutes that contain sediment with short (< 10 kyr) residence times, we can assume that higher δ^7Li_{clay} values indicate high weathering rates or longer weathering durations. As for OC contents, assuming a narrow range of primary productivity at a given locality, a wide span instead necessitates having variable transformation rates of OC_{slow}. This can be accomplished by differing the inherent rates of OC_{slow} transformation, $k_{C_{slow}}$, or differing the sensitivity of OC_{slow} stability to clay mineral formation, n (Eq. (4)), where a decrease in either $k_{C_{slow}}$ or n will enable more OC_{slow} to accumulate over a given time interval (Fig. 6B). The values of $k_{C_{slow}}$ or n can plausibly vary within a landscape because conditions that affect OC transformation like sediment age and age distribution (Boudreau and Ruddick, 1991), OC molecular form (Boye et al., 2017), soil mineralogy (Lawrence et al., 2015), and soil redox state can also vary within a landscape.

When OC-Li isotope arrays (Fig. 2) are compared with model predictions (Fig. 6B), there are areas where heterogeneous biogeochemical cycling may be a viable explanation at a given locality. For example, in this model framework, sediment with low δ^7Li values and high OC would represent a soil formation pathway where 1) clay protection is highly effective (low n) and/or OC is more recalcitrant (low $k_{C_{slow}}$) and 2) timescales of biogeochemical cycling are short and/or limited amounts of clay form (Fig. 5, 6B). Although the coincidence of low amounts of clay formation and high OC stabilization seems counterintuitive, these conditions are formally possible and supported widely by observations of soil chronosequences. In the Hawaii chronosequence, for instance, a young soil profile (20 kyr) with low amounts of crystalline clay (Torn et al., 1997) has the lowest average δ^7Li value of all the profiles (Ryu et al., 2014). Previous authors identify the central role of amorphous allophane and imogolite in this profile that enable high OC accumulation in such early stages of soil development (Torn et al., 1997). So, the differing OC sensitivity n may indicate a mineralogical control on these Li isotope-OC trends. However, there are limits to these model predictions. For example, the sample with the lowest OC content and highest δ^7Li value from Rio Bermejo overlaps models with a high relative duration of weathering and high relative amounts of clay formation (Figs. 2B, 6B). Yet, this sample has the highest sand content and appears compositionally most representative of bedrock. The negative correlation would still hold if this sample was excluded from the Rio Bermejo array (Fig. 2B), but its occurrence delineates the narrower application of this model framework to samples with low sand content. We thus conclude that although biogeochemical cycling will certainly vary within a given landscape and at different soil depths, fluvial processes may homogenize and obfuscate the extent of biogeochemical processes.

Table 1
Relevant metrics for OC cycling, climate, and bedrock chemistry. Values are absolute ranges or mean annual values. Sources are listed below each quantity. GPP: gross primary productivity; MAT: mean annual temperature; MAP: mean annual precipitation.

	Rio Bermejo	Little Deschutes	Hawaii
$\delta^{13}C$ (‰ VPDB)	-27.1 to -25.2	-29.8 to -27.4	
	(Scheingross et al., 2021)	This study	
Fm C	0.78–0.91	0.84–1.04	0.46–1.10
	(Repasch et al., 2021)	This study	(Torn et al., 1997)
GPP ($g \cdot m^{-2} \cdot yr^{-1}$)	600–2000	620–1300	2500–5500
	(Bi et al., 2022)	(Bi et al., 2022)	(Bi et al., 2022; Litton et al., 2007)
C (wt.%)	0.1–0.4	7.9–16.7	2.2–15.4
	(Repasch et al., 2021)	This study	(Torn et al., 1997)
C/N ($wt.\% \cdot wt.\%^{-1}$)	3–10	14–46	7–27
	This study	This study	(Mikutta et al., 2009)
MAT (°C)	22	8	25
	(Harris et al., 2014)	(Gannett, 2004)	(Torn et al., 1997)
MAP ($mm \cdot yr^{-1}$)	1200	1200	1700–3000
	(Harris et al., 2014)	(Gannett, 2004)	(Torn et al., 1997)
Bedrock type	Sedimentary	Volcanic	Basaltic
Landscape element	Floodplain	Floodplain	Hillslope

5.2. The unifying role of clay mineral formation

Despite the nuances that could explain the relationship between δ^7Li values and OC content at a given locality, the distinct range of values across each of the localities supports broader governing controls of silicate weathering and OC cycling. Climate, bedrock chemistry, and mineral supply fundamentally limit silicate weathering intensity and potential OC storage in soil (Slessarev et al., 2022; Roering et al., 2023). Leveraging the wide span of rock types, climates, and landscape elements characterizing the three study sites, we infer differing impacts of these controls on sediment OC contents and δ^7Li values. For instance, Hawaii and the Little Deschutes contain sediment/soil with similarly high OC contents (Fig. S5; Table 1) despite the former being tropical and the latter being temperate. The low input of OC from primary productivity and high export of DOC (as inferred by high soil C/N (Aitkenhead and McDowell, 2000)) in the Little Deschutes indicate that clay protection or high OC recalcitrance should sustain high sediment OC contents. Soils in Hawaii, with higher primary productivity and less DOC export than Little Deschutes, could sustain its OC content with less sensitive clay protection. The Rio Bermejo has high primary productivity (Table 1) yet soil and river sediment with comparatively low OC contents (Fig. S6), suggesting significant oxidation of OC (Scheingross et al., 2021) despite evidence of clay-mediated OC protection (Repasch et al., 2021). Bedrock chemistry distinguishes Rio Bermejo from Hawaii and the Little Deschutes (Table 1) and likely plays a central role in the OC content disparity, especially given the lack of evidence to support widely varying OC form and recalcitrance across the sites. The high weatherability of extrusive igneous bedrock and their high cation content, irrespective of climate and the supply of fresh minerals, could support swift production of clay minerals that then occlude OC (Slessarev et al., 2022; Torn et al., 1997). The similarly steep slopes of their OC-Li isotope arrays may support that their watershed-average capacity to occlude OC is related to their bedrock chemistry (Fig. 2, 6B).

Furthermore, the disparity in δ^7Li values between the Little Deschutes and Rio Bermejo may point to a mineralogical control on Li isotope fractionation factors. The formation of amorphous phases and halloysite is associated with the lowest Li isotope fractionation factors (Winnick et al., 2022), potentially explaining the exceptionally low δ^7Li_{fine} values in the Little Deschutes. Smectite, which is the abundant weathering product in the Rio Bermejo, tends to have comparable or more positive fractionation factors (Hindshaw et al., 2019) compared to halloysite. However, the wide range of δ^7Li values across the three sites may also illustrate the viable influence of climate and primary productivity on weathering across the sites. Low δ^7Li_{clay} values observed in cool, temperate Little Deschutes indicate limited net clay formation whereas high δ^7Li_{clay} values in subtropical Rio Bermejo and high δ^7Li_{soil} values in tropical Hawaii indicate high relative amounts of clay formation. The large differences between primary productivity and C/N at both Rio Bermejo and Hawaii imply that OC-enhanced mineral dissolution could facilitate the high relative amounts of clay formation. Moreover, the limited erosion of the Hawaii ridgetop soils and the low-relief floodplains in the Rio Bermejo likely yields long mineral residence times that encourage more intense weathering.

Ultimately, if sediment from Rio Bermejo are intensely weathered and have low OC content whereas those from Little Deschutes are not intensely weathered and have high OC content, their discrepancy reinforces the idea that the crystallinity and type of clay that forms in soil strongly relates to the magnitude of OC stabilization (Torn et al., 1997) rather than clay formation alone. Newly paired measurements of Li isotope ratios and OC content illuminate that while bedrock chemistry and climate together dictate reaction progress, bedrock chemistry more strongly imposes constraints on reaction stoichiometry and thus weathering products. Therefore, we assert that bedrock chemistry establishes the primary coupling of silicate weathering and OC cycling in soil on millennial timescales and sets the potential of soil to sequester atmospheric CO_2. To make globally relevant predictions about OC stability in soil, however, clay mineral dissolution and formation rates in natural systems need to be improved. Recent modeling efforts highlight that uncertainty in clay mineral formation rates can have an outsize effect on where in landscapes we expect OC to be best protected by secondary minerals (Roering et al., 2023), underscoring the need for these rates to be refined. In lieu of using more sophisticated models of soil formation that are calibrated to soil profile data (Maher et al., 2009), measurements of Li isotope ratios of river solutes or sediment may offer an alternative, useful constraint on the timing and magnitude of clay mineral formation at the watershed scale. These measurements, paired with more detailed characterizations of organic matter, should improve the quantification of clay formation and OC transformation rates that when incorporated into Earth system models can advance our quantitative understanding of past climates and future climate projections (IPCC, 2022).

CRediT authorship contribution statement

Evan J. Ramos: Writing – original draft, Visualization, Software, Investigation, Funding acquisition, Formal analysis, Data curation, Conceptualization. **William J. Larsen:** Writing – review & editing, Software, Investigation. **Yi Hou:** Writing – review & editing, Software, Investigation. **Sebastian Muñoz:** Writing – review & editing, Funding acquisition. **Preston Cosslett Kemeny:** Writing – review & editing, Software, Investigation. **Joel S. Scheingross:** Writing – review & editing, Data curation. **Marisa N. Repasch:** Writing – review & editing,

Resources. **Niels Hovius:** Resources. **Dirk Sachse:** Resources. **Daniel E. Ibarra:** Writing – review & editing, Supervision, Resources, Project administration, Investigation, Funding acquisition, Conceptualization. **Mark A. Torres:** Writing – review & editing, Supervision, Software, Resources, Project administration, Investigation, Funding acquisition, Conceptualization.

Declaration of competing interest

The authors declare that they have no known competing financial interests or personal relationships that could have appeared to influence the work reported in this paper.

Data availability

All data is available in supplementary material.

Acknowledgements

We are grateful to Amanda Madson and Meria Page at the U.S. Forest Service field office in Crescent, OR for assistance with and timely assessment of permit requests, to Staci Loewy and Aaron Satkoski for assistance with lithium isotope measurements, to Jesse Miller for assistance with field work during 2022 and soil C analyses, to Carrie Masiello for helpful discussions, to three anonymous referees whose input improved the manuscript, and to Huiming Bao for careful editorial handling and helpful scientific input. This work was supported by NSF-EAR-2053056 (to Ramos), NSF-EAR-2017106 (to Torres), seed grants from the Institute at Brown for Environment and Society (to Muñoz and Ibarra), and the TC Chamberlin Fellowship at the University of Chicago and NSF-EAR-2204376 (to Kemeny). Additional funding by the Helmholtz Association of German Research Centres under the Program "Changing Earth - Sustaining our Future" and the Deutsche Forschungsgemeinschaft (DFG) Grant STR 373/34–1 and the Brandenburg Ministry of Sciences, Research and Cultural Affairs (Germany) through the international research training group IGK2018 (StRATEGy), led by Manfred Strecker, supported work in Argentina. All code for data processing, figure generation, and numerical modeling can be found in this GitHub repository: https://github.com/ejramos/Li-OC.

Appendix A. Supplementary material

Supplementary material related to this article can be found online at https://doi.org/10.1016/j.epsl.2024.118584.

References

Aitkenhead, J., McDowell, W.H., 2000. Soil C:N ratio as a predictor of annual riverine DOC flux at local and global scales. Glob. Biogeochem. Cycles 14, 127–138.
Andrews, E., von Strandmann, P.A.P., Fantle, M.S., 2020. Exploring the importance of authigenic clay formation in the global Li cycle. Geochim. Cosmochim. Acta 289, 47–68.
Beerling, D.J., Kantzas, E.P., Lomas, M.R., et al., 2020. Potential for large-scale CO_2 removal via enhanced rock weathering with croplands. Nature 583, 242–248.
Berner, R.A., Caldeira, K., 1997. The need for mass balance and feedback in the geochemical carbon cycle. Geology 25, 955.
Berner, R.A., Lasaga, A.C., Garrels, R.M., 1983. The carbonate-silicate geochemical cycle and its effect on atmospheric carbon dioxide over the past 100 million years. Am. J. Sci. 283, 641–683.
Bi, W., He, W., Zhou, Y., et al., 2022. A global 0.05 dataset for gross primary production of sunlit and shaded vegetation canopies from 1992 to 2020. Sci. Data 9, 213.
Bouchez, J., von Blanckenburg, F., Schuessler, J.A., 2013. Modeling novel stable isotope ratios in the weathering zone. Am. J. Sci. 313, 267–308.
Boudreau, B.P., Ruddick, B.R., 1991. On a reactive continuum representation of organic matter diagenesis. Am. J. Sci. 291, 507–538.
Boye, K., Noël, V., Tfaily, M.M., et al., 2017. Thermodynamically controlled preservation of organic carbon in floodplains. Nat. Geosci. 10, 415–419.
Chadwick, O.A., Chorover, J., 2001. The chemistry of pedogenic thresholds. Geoderma 100, 321–353.
Chadwick, O.A., Kelly, E.F., Merritts, D.M., Amundson, R.G., 1994. Carbon dioxide consumption during soil development. Biogeochemistry 24, 115–127.
Chadwick, O.A., Derry, L.A., Vitousek, P.M., 1999. Changing sources of nutrients during four million years of ecosystem development. Nature 397, 491–497.
Chen, Z., Ding, Z., Yang, S., et al., 2023. Strong coupling between carbon cycle, climate, and weathering during the Paleocene-Eocene Thermal Maximum. Geophys. Res. Lett. 50, e2023GL102897.
Dellinger, M., Gaillardet, J., Bouchez, J., et al., 2014. Lithium isotopes in large rivers reveal the cannibalistic nature of modern continental weathering and erosion. Earth Planet. Sci. Lett. 401, 359–372.
Dellinger, M., Gaillardet, J., Bouchez, J., et al., 2015. Riverine Li isotope fractionation in the Amazon River basin controlled by the weathering regimes. Geochim. Cosmochim. Acta.
Dellinger, M., Bouchez, J., Gaillardet, J., Faure, L., Moureau, J., 2017. Tracing weathering regimes using the lithium isotope composition of detrital sediments. Geology 45, 411–414.
Doetterl, S., Berhe, A.A., Nadeu, E., Wang, Z., Sommer, M., Fiener, P., 2016. Erosion, deposition and soil carbon: a review of process-level controls, experimental tools and models to address C cycling in dynamic landscapes. Earth-Sci. Rev. 154, 102–122.
Dosseto, A., Vigier, N., Joannes-Boyau, R.C., Moffat, I., Singh, T., Srivastava, P., 2015. Rapid response of silicate weathering rates to climate change in the Himalaya. Geochem. Perspect. Lett.
Drever, J.I., 1994. The effect of land plants on weathering rates of silicate minerals. Geochim. Cosmochim. Acta 58, 2325–2332.
Dudas, M., Harward, M., 1975. Weathering and authigenic halloysite in soil developed in Mazama ash. Soil Sci. Soc. Am. J. 39, 561–566.
Fang, Q., Lu, A., Hong, H., et al., 2023. Mineral weathering is linked to microbial priming in the critical zone. Nat. Commun. 14, 345.
Ferrier, K.L., Kirchner, J.W., 2008. Effects of physical erosion on chemical denudation rates: a numerical modeling study of soil-mantled hillslopes. Earth Planet. Sci. Lett. 272, 591–599.
Frings, P.J., Schubring, F., Oelze, M., von Blanckenburg, F., 2021. Quantifying biotic and abiotic Si fluxes in the Critical Zone with Ge/Si ratios along a gradient of erosion rates. Am. J. Sci. 321, 1204–1245.
Gannett, M.W., 2004. Simulation of regional ground-water flow in the upper Deschutes Basin, Oregon, vol. 3. US Department of the Interior, US Geological Survey.
Golla, J.K., Kuessner, M.L., Henehan, M.J., Bouchez, J., Rempe, D.M., Druhan, J.L., 2021. The evolution of lithium isotope signatures in fluids draining actively weathering hillslopes. Earth Planet. Sci. Lett. 567, 116988.
Hahm, W.J., Riebe, C.S., Lukens, C.E., Araki, S., 2014. Bedrock composition regulates mountain ecosystems and landscape evolution. Proc. Natl. Acad. Sci. USA 111, 3338–3343.
Harris, I., Jones, P.D., Osborn, T.J., Lister, D.H., 2014. Updated high-resolution grids of monthly climatic observations—the CRU TS3. 10 Dataset. Int. J. Climatol. 34, 623–642.
Heckman, K., Hicks Pries, C.E., Lawrence, C.R., et al., 2022. Beyond bulk: density fractions explain heterogeneity in global soil carbon abundance and persistence. Glob. Change Biol. 28, 1178–1196.
Hemingway, J.D., Rothman, D.H., Grant, K.E., et al., 2019. Mineral protection regulates long-term global preservation of natural organic carbon. Nature 570, 228–231.
Hilton, R.G., West, A.J., 2020. Mountains, erosion and the carbon cycle. Nat. Rev. Earth Environ. 1, 284–299.
Hindshaw, R.S., Tosca, R., Goût, T.L., Farnan, I., Tosca, N.J., Tipper, E.T., 2019. Experimental constraints on Li isotope fractionation during clay formation. Geochim. Cosmochim. Acta 250, 219–237.
Hotchkiss, S., Vitousek, P.M., Chadwick, O.A., Price, J., 2000. Climate cycles, geomorphological change, and the interpretation of soil and ecosystem development. Ecosystems 3, 522–533.
Huang, K.F., You, C.F., Liu, Y.H., Wang, R.M., Lin, P.Y., Chung, C.H., 2010. Low-memory, small sample size, accurate and high-precision determinations of lithium isotopic ratios in natural materials by MC-ICP-MS. J. Anal. At. Spectrom. 25, 1019–1024.
Huh, Y., Chan, L.H., Zhang, L., Edmond, J.M., 1998. Lithium and its isotopes in major world rivers: implications for weathering and the oceanic budget. Geochim. Cosmochim. Acta 62, 2039–2051.
Huh, Y., Chan, L.H., Oa, Chadwick, 2004. Behavior of lithium and its isotopes during weathering of Hawaiian basalt. Geochem. Geophys. Geosyst. 5, 1–22.
IPCC, 2022. Climate Change 2022: Impacts, Adaptation and Vulnerability. Summary for Policymakers. Cambridge University Press, Cambridge, UK and New York, USA, pp. 3–33.
Lawrence, C., Harden, J., Maher, K., 2014. Modeling the influence of organic acids on soil weathering. Geochim. Cosmochim. Acta 139, 487–507.
Lawrence, C.R., Harden, J.W., Xu, X., Schulz, M.S., Trumbore, S.E., 2015. Long-term controls on soil organic carbon with depth and time: a case study from the Cowlitz River Chronosequence, WA USA. Geoderma 247–248, 73–87.
Li, W., Liu, X.M., Chadwick, O.A., 2020. Lithium isotope behavior in Hawaiian regoliths: soil-atmosphere-biosphere exchanges. Geochim. Cosmochim. Acta 285, 175–192.
Liang, C., Schimel, J.P., Jastrow, J.D., 2017. The importance of anabolism in microbial control over soil carbon storage. Nat. Microbiol. 2, 1–6.
Litton, C.M., Raich, J.W., Ryan, M.G., 2007. Carbon allocation in forest ecosystems. Glob. Change Biol. 13, 2089–2109.
Lupker, M., France-Lanord, C., Galy, V., et al., 2012. Predominant floodplain over mountain weathering of Himalayan sediments (Ganga basin). Geochim. Cosmochim. Acta 84, 410–432.

Maher, K., von Blanckenburg, F., 2023. The circular nutrient economy of terrestrial ecosystems and the consequences for rock weathering. Front. Environ. Sci., 10.
Maher, K., Steefel, C.I., White, A.F., Stonestrom, D.A., 2009. The role of reaction affinity and secondary minerals in regulating chemical weathering rates at the Santa Cruz Soil Chronosequence, California. Geochim. Cosmochim. Acta 73, 2804–2831.
Malkowski, M.A., Sharman, G.R., Johnstone, S.A., Grove, M.J., Kimbrough, D.L., Graham, S.A., 2019. Dilution and propagation of provenance trends in sand and mud: geochemistry and detrital zircon geochronology of modern sediment from central California (USA). Am. J. Sci. 319, 846–902.
Masiello, C.A., Chadwick, O.A., Southon, J., Torn, M.S., Harden, J.W., 2004. Weathering controls on mechanisms of carbon storage in grassland soils. Glob. Biogeochem. Cycles 18, 1–9.
McGlue, M.M., Smith, P.H., Zani, H., et al., 2016. An integrated sedimentary systems analysis of the Río Bermejo (Argentina): megafan character in the overfilled Southern Chaco foreland basin. J. Sediment. Res. 86, 1359–1377.
Mikutta, R., Schaumann, G.E., Gildemeister, D., et al., 2009. Biogeochemistry of mineral–organic associations across a long-term mineralogical soil gradient (0.3–4100 kyr), Hawaiian Islands. Geochim. Cosmochim. Acta 73, 2034–2060.
Nagy, K.L., Blum, A.E., Lasaga, A.C., 1991. Dissolution and precipitation kinetics of kaolinite at 80 °C and pH 3: the dependence on solution saturation state. Am. J. Sci. 291, 649–686.
Qi, H.P., Taylor, P., Berglund, M., De Bièvre, P., 1997. Calibrated measurements of the isotopic composition and atomic weight of the natural Li isotopic reference material IRMM-016. Int. J. Mass Spectrom. Ion Process. 171, 263–268.
Ramos, E.J., Breecker, D.O., Barnes, J.D., et al., 2022. Swift weathering response on floodplains during the Paleocene-Eocene Thermal Maximum. Geophys. Res. Lett. 49, e2021GL097436.
Rasmussen, C., Heckman, K., Wieder, W.R., et al., 2018. Beyond clay: towards an improved set of variables for predicting soil organic matter content. Biogeochemistry 137, 297–306.
Repasch, M., Wittmann, H., Scheingross, J.S., et al., 2020. Sediment transit time and floodplain storage dynamics in alluvial rivers revealed by meteoric ^{10}Be. J. Geophys. Res., Earth Surf. 125, e2019JF005419.
Repasch, M., Scheingross, J.S., Hovius, N., et al., 2021. Fluvial organic carbon cycling regulated by sediment transit time and mineral protection. Nat. Geosci. 14, 842–848.
Repasch, M., Scheingross, J.S., Cook, K.L., et al., 2023. Lithospheric flexure controls on geomorphology, hydrology, and river chemistry in the Andean foreland basin. AGU Adv. 4, e2023AV000924.
Roering, J.J., Hunter, B.D., Ferrier, K.L., et al., 2023. Quantifying erosion rates and weathering pathways that maximize soil organic carbon storage. Biogeochemistry, 1–15.
Ryu, J.S., Vigier, N., Lee, S.W., Lee, K.S., Chadwick, O.A., 2014. Variation of lithium isotope geochemistry during basalt weathering and secondary mineral transformations in Hawaii. Geochim. Cosmochim. Acta 145, 103–115.
Scheingross, J.S., Repasch, M.N., Hovius, N., et al., 2021. The fate of fluvially-deposited organic carbon during transient floodplain storage. Earth Planet. Sci. Lett. 561, 116822.
Schmidt, M.W.I., Torn, M.S., Abiven, S., et al., 2011. Persistence of soil organic matter as an ecosystem property. Nature 478, 49–56.
Slessarev, E.W., Chadwick, O.A., Sokol, N.W., Nuccio, E.E., Pett-Ridge, J., 2022. Rock weathering controls the potential for soil carbon storage at a continental scale. Biogeochemistry 157, 1–13.
Spohn, M., Klaus, K., Wanek, W., Richter, A., 2016. Microbial carbon use efficiency and biomass turnover times depending on soil depth—implications for carbon cycling. Soil Biol. Biochem. 96, 74–81.
Straub, K.M., Duller, R.A., Foreman, B.Z., Hajek, E.A., 2020. Buffered, incomplete, and shredded: the challenges of reading an imperfect stratigraphic record. J. Geophys. Res., Earth Surf. 125, e2019JF005079.
Talbot, C.J., Bolster, D., Medvigy, D., Jones, S.E., 2022. A terrestrial-aquatic model reveals cross-scale interactions regulate lateral dissolved organic carbon transport from terrestrial ecosystems. J. Geophys. Res., Biogeosci. 127, e2021JG006604.
Tipping, E., Rey-Castro, C., Bryan, S.E., Hamilton-Taylor, J., 2002. Al (III) and Fe (III) binding by humic substances in freshwaters, and implications for trace metal speciation. Geochim. Cosmochim. Acta 66, 3211–3224.
Torn, M.S., Trumbore, S.E., Oa, Chadwick, Vitousek, P.M., Hendricks, D.M., 1997. Mineral control of soil organic carbon storage and turnover. Nature 389, 3601–3603.
Walker, J., Hays, P.B., Kasting, J.F., 1981. A negative feedback mechanism for the long-term stabilization of the Earth's surface temperature. J. Geophys. Res. 86, 9776–9782.
White, A.F., Brantley, S.L., 2003. The effect of time on the weathering of silicate minerals: why do weathering rates differ in the laboratory and field? Chem. Geol. 202, 479–506.
Winnick, M.J., Maher, K., 2018. Relationships between CO_2, thermodynamic limits on silicate weathering, and the strength of the silicate weathering feedback. Earth Planet. Sci. Lett. 485, 111–120.
Winnick, M.J., Druhan, J.L., Maher, K., 2022. Weathering intensity and lithium isotopes: a reactive transport perspective. Am. J. Sci. 322, 647–682.
Zhu, G., Ma, J., Wei, G., et al., 2023. Lithium isotope fractionation during the weathering of granite: responses to pH. Geochim. Cosmochim. Acta.